Modeling structural deformation and failure in fluid-structure interaction with WC-TLSPH

Haitao Wu[1,2,3], Shenglong Gu[1,2,3]*, Lirong Tian[1,2,3], Jiaye Li[4,5]*, Chen Chen[4,5] and Chi Zhang[6]

[1]School of Water Resources and Electric Power, Qinghai University, Xining, China, [2]Laboratory of Ecological Protection and High-Quality Development in the Upper Yellow River, Xining, China, [3]Key Laboratory of Water Ecology Remediation and Protection at Headwater Regions of Big Rivers, Ministry of Water Resources, Xining, China, [4]School of Environment and Civil Engineering, Dongguan University of Technology, Dongguan, China, [5]Center for Hydrosphere Science, Key Laboratory of Engineering Software, Dongguan University of Technology, Dongguan, China, [6]TUM School of Engineering and Design, Technical University of Munich, Garching, Germany

In this paper, the coupled weakly compressible (WC) and total Lagrangian (TL) smoothed particle hydrodynamics (SPH) model based on the open-source multi-physics and multi-resolution SPHinXsys library is used to simulate the structural deformation and failure problem in fluid-structure interaction (FSI). Aiming at the problem that the original TLSPH method could not simulate the cracks and their propagation, the fracture model based on TLSPH is established, and then verified by fast-loading and slow-loading cases respectively. With the fracture model in hand, the TLSPH method is coupled with the WCSPH method to simulate the breaking dam flow impacting on an elastic/elastoplastic baffle. The comparison with the literature data shows that the present coupled WC-TLSPH model can accurately simulate the FSI problem where figurative fracture process is involved, indicating the compromising potential of the established model to simulate the elastoplastic structural failure in scientific and industrial applications.

Introduction

Fluid-structure interaction (FSI) is a common phenomenon in various engineering problems which characterized by dramatic change of the flow domain size and shape with the movement or deformation of the structure, leading to its numerical solution is relatively complicated, and of great significance to ensure the safe and stable operation of the structure. Therefore, one of the primary aims of solving FSI problem is to accurately simulate the changing state of structure, and even its failure accurately.

The computational mechanics is considered to be the main approach for solving FSI problems because of its flexibility, and it has made great progress in the past few decades. From a solution point of view, there are generally two main solutions, *i.e.*, a direct solution and an indirect solution (Salehizadeh and Shafiei, 2022). The direct solution refers to

FIGURE 1
Flow chart for the WC-TLSPH model.

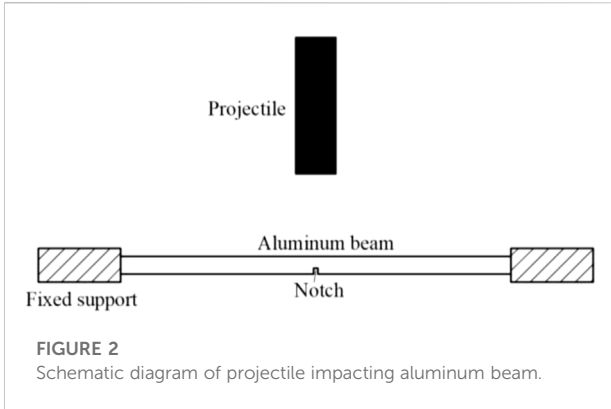With the development of meshless methods in the last decades, alternative solutions have been merged for solving FSI problems. Smoothed particle hydrodynamics (SPH) is a representative meshless method, originally proposed by Lucy, Gingold and Monaghan (Monaghan, 1992) and applied to astrophysics applications. It is a truly meshless, Lagrangian particle method in which the computational domain is discretized into a series of material points carry the field variables such as density, stress tensor and velocity, *etc*. Thanks to its pure Lagrangian property, it has unique advantages in dealing with large deformations, free surfaces and interfaces, and has been applied to in a wide range of fluid and solid computational problems (Bui et al., 2008; Shi et al., 2017; Shi et al., 2019; Gabreil et al., 2022; Gu et al., 2022; Zhang et al., 2022). Zheng et al. (2022) used the SPH method to model the FSI problem of icebreaker sailing in the ice river, where the updated Lagrangian SPH (ULSPH) formulation is used to solve the solid mechanics formulation. However, the using of ULSPH method in which the current configuration is used as the reference will lead to the problem of tensile instability hindering its application to a large extent because it leads to particle sticking and unphysical fracture. Although the application of kernel function reconstruction (Johnson and Beissel, 1996), artificial stress (Gray et al., 2001), generalized transport-velocity formulation (Zhang et al., 2017b) and other methods can solve the problem of tensile instability to a certain degree, these methods introduce additional model parameters, and the choice of these parameters has side effect on the simulation results. According to Belytschko et al. (2000), the use of Euler kernel in ULSPH is the main reason for tensile instability. To fundamentally solve the problem of tensile instability, it is necessary to avoid the use of Euler kernel, *viz*. the total Lagrangian SPH (TLSPH) which applies the Lagrangian kernel and being entirely free of tensile instability. The so-called Lagrangian kernel is to perform particle pairing and calculate the kernel function gradient according to the initial configuration only once before the calculation starts, which means that TLSPH is not suitable for the solution of fluid dynamics where the deformation of particles in the flow process is relatively large. Therefore, by the coupling of weakly compressible SPH (WCSPH) and TLSPH, respectively solving fluid dynamics and solid mechanics, the solution of FSI problems can be well realized.

In terms of the coupling of WCSPH and TLSPH, some scholars have carried out a series of research and achieved certain achievements (He et al., 2017; Zhan et al., 2019; Zhang et al., 2021a). However, in the research of FSI problems where the fracture and failure of materials are involved, the original TLSPH method cannot handle the cracking and fragmentation problems (Islam and Peng, 2019). In order to study the failure of structures in FSI and further expand the application of the TLSPH, the fracture model coupled with TLSPH is established based on the SPHinXsys (https://www.sphinxsys.org) in this paper. SPHinXsys is an open-source multi-physics and multi-resolution library acronym from Smoothed Particle Hydrodynamics for industrial complex systems. It provides open-source C++ APIs for physical accurate simulation and aims to model and to optimize coupled industrial dynamic

solving both fluid and structure dynamics synchronously, while the indirect solution refers to calculating the stress on the structure by solving the fluid dynamics firstly, and then imposing the stress as the boundary condition to solve the deformation of the structure. In terms of specific methods, several grid-based analytical/computational methods, *e.g.* finite difference method (FDM) (Sugiyama et al., 2011), finite element method (FEM) (Mitra andSinhamahapatra, 2008) and finite volume method (FVM) (Lv et al., 2007), have been applied and achieved certain degree of success. However, in violent FSI contact problems, the grid-based methods encounter serious mesh distortion and mesh redrawing problems. To address these issues, the Arbitrary Lagrangian Eulerian (ALE) (Sarrate et al., 2001) is proposed by modelling the structure with the fully Lagrangian formula, whereas a particular modification is required for the precision definition of interface and free surfaces (Salehizadeh and Shafiei, 2022).

systems including fluid, solid, multi-body dynamics (Zhang et al., 2021b). In addition, SPHinXsys shows impressive computational performance thanks to implementing shared-memory parallel programming on multi-core processors by applying Threading Building Blocks (TBB) library developed by Intel (Zhang et al., 2021c).

This paper is structured as follows. The theory and fundamentals of WCSPH, TLSPH and WC-TLSPH are briefly summarized in Section 2. The fracture model for TLSPH is introduced in Section 3. The fast-loading fracture case of crack propagation in notched beam and the slow-loading fracture case of three-point bending of ice beam based on TLSPH, as well as the further model validations of breaking dam on elastic and elastoplastic baffles are investigated in Section 4 and finally the conclusions and future works are noted in Section 5.

Theory of WC-TLSPH

Scheme of WCSPH

The Navier-Stokes equations (N-S equations) for fluid dynamics in the Lagrangian framework can be written as

$$\begin{cases} \dfrac{d\rho}{dt} = -\rho\nabla \cdot \mathbf{v} \\ \dfrac{d\mathbf{v}}{dt} = -\dfrac{1}{\rho}\nabla P + \mathbf{g} \end{cases} \quad (1)$$

where ρ is the density, $\mathbf{v}$ the velocity, P the pressure, $\mathbf{g}$ the gravity, $\frac{d}{dt} = \frac{\partial}{\partial t} + \nabla \cdot \mathbf{v}$ stands for the material derivative. For the weakly compressible fluid, the governing equations above can be closed by an artificial equation of state (EoS) reads

$$P = c^2 (\rho - \rho_0) \quad (2)$$

where ρ_0 is the reference density and the artificial sound speed $c = 10U_{max}$ (U_{max} is the anticipated maximum flow speed) can ensure the density change is about 1% (Morris et al., 1997).

According to the discrete formula of the SPH method, the WCSPH method based on Riemann solver is applied in SPHinXsys to achieve stabilized simulations. Following Zhang et al. (2017a), one-dimensional Riemann problem is constructed along the interacting line of particle i and j, then discretization of the N-S equation can be rewritten as

$$\begin{cases} \dfrac{d\rho_i}{dt} = 2\rho_i \sum_j \dfrac{m_j}{\rho_j} \left(U^\star - \mathbf{v}_i \mathbf{e}_{ij} \right) \dfrac{\partial W_{ij}}{\partial r_{ij}} \\ \dfrac{d\mathbf{v}_i}{dt} = -2 \sum_j m_j \dfrac{P^\star}{\rho_i \rho_j} \nabla_i W_{ij} + \mathbf{g} \end{cases} \quad (3)$$

where m is the particle mass, W the smooth kernel function, $\nabla_i W_{ij}$ the gradient of the kernel function from particle i to particle j, $U^\star$ and $P^\star$ represents the solutions of an inter-particle Riemann problem from a low-dissipation Riemann solver can be calculated by

$$\begin{cases} U^\star = \bar{U} + \dfrac{1}{2} \dfrac{(P_L - P_R)}{\bar{\rho} c_0} \\ P^\star = \bar{P} + \dfrac{1}{2}\bar{\rho} c_0 (U_L - U_R) \end{cases} \quad (4)$$

where the subscprpts L and R represent the left and right states in Riemann problems and the initial L and R states are on particle i and j respectively, i.e., $(\rho_L, U_L, P_L) = (\rho_i, \mathbf{v}_i \cdot \mathbf{e}_{ij}, P_i)$, $(\rho_R, U_R, P_R) = (\rho_j, \mathbf{v}_j \cdot \mathbf{e}_{ij}, P_j)$, $\mathbf{e}_{ij}$ is unit vector, $\bar{U} = (U_L + U_R)/2$ and $\bar{P} = (P_L + P_R)/2$ are inter-particle averages.

Scheme of TLSPH

For the solid mechanics, we follow the Lagrangian framework where all the conservation equations are expressed in terms of the initial coordinates $\mathbf{R}$, which are taken as the reference configuration. Then the displacement $\mathbf{s}$ of any material point can be defined as

$$\mathbf{s} = \mathbf{r} - \mathbf{R} \quad (5)$$

where $\mathbf{r}$ stands for the current, viz. deformed configuration. The conservation equations of mass and momentum read

$$\begin{cases} \rho = \rho^0 \dfrac{1}{J} \\ \dfrac{d\mathbf{v}}{dt} = \dfrac{1}{\rho^0} \nabla^0 \cdot \mathbf{P} + \rho^0 \mathbf{g} \end{cases} \quad (6)$$

where the superscripts 0 indicates the values expressed in the initial configuration, J is the Jacobian given by $J = \det(\mathbf{F})$ with $\mathbf{F}$ denoting the deformation tensor, $\mathbf{P}$ stands for the first Piola-Kirchhoff stress tensor and the relation between $\mathbf{P}$ and Cauchy stress tensor σ can be written as:

$$\mathbf{P} = J\sigma\mathbf{F}^{-T} \quad (7)$$

Another important stress tensor $\mathbf{S}$, i.e. the second Piola-Kirchhoff stress tensor, is given by
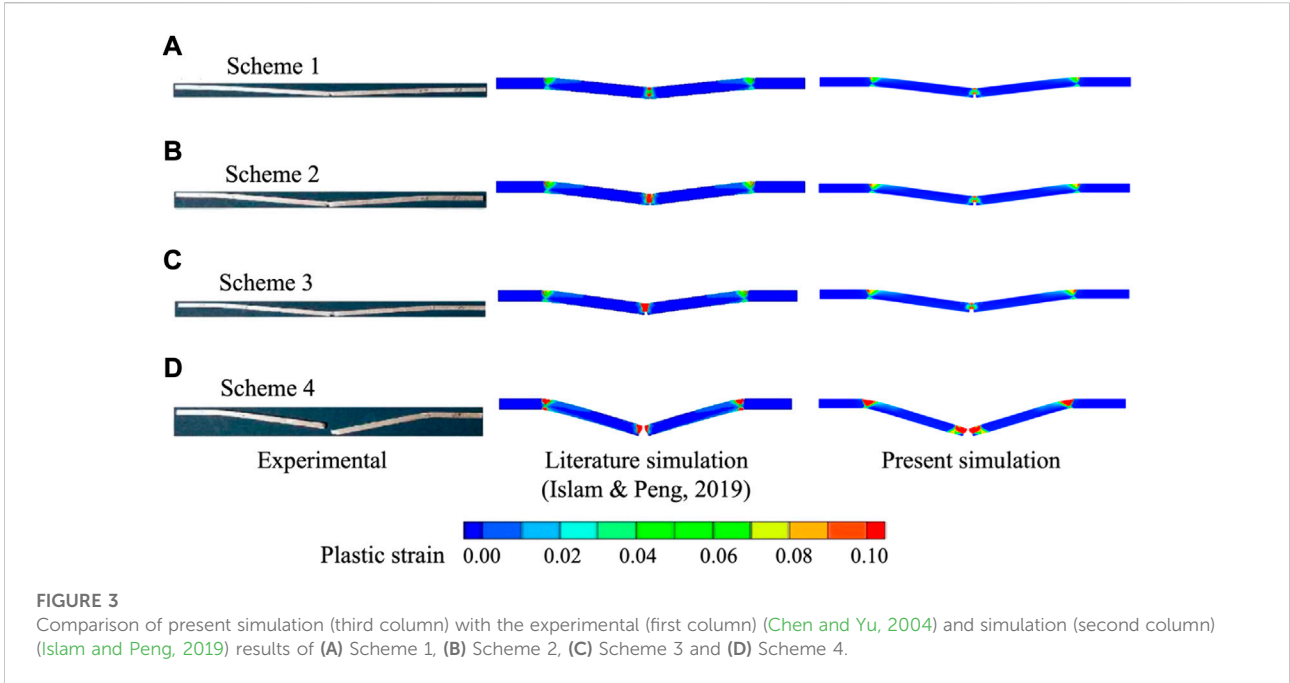
FIGURE 3
Comparison of present simulation (third column) with the experimental (first column) (Chen and Yu, 2004) and simulation (second column) (Islam and Peng, 2019) results of **(A)** Scheme 1, **(B)** Scheme 2, **(C)** Scheme 3 and **(D)** Scheme 4.

TABLE 1 The material properties of the aluminum beam.

Density (kg/m^3)	Elastic modulus (GPa)	Poisson's ratio (/)	Yield stress (MPa)	Hardening modulus (GPa)
2,680	68.95	0.33	277.8	0.466

TABLE 2 The details of simulation scheme.

Scheme number	Scheme 1	Scheme 2	Scheme 3	Scheme 4
Notch type	I	I	II	II
Initial velocity of projectile (m/s)	14.2	18.2	19.2	27.1

$$\mathbf{S} = J\mathbf{F}^{-1}\sigma\mathbf{F}^{-T} \qquad (8)$$

Then, the first Piola-Kirchhoff stress tensor $\mathbf{P}$ can also be expressed as $\mathbf{P} = \mathbf{F}\mathbf{S}$. Particularly, the second Piola-Kirchhoff stress tensor $\mathbf{S}$ can be calculated by the constitutive equation.

For the discretization of Eq. 6, a kernel correction matrix $\mathbf{B}^0$ is introduced to ensure the first-order consistency of the TLSPH methods as

$$\mathbf{B}_i^0 = \left(\sum_j V_j \left(\mathbf{r}_j^0 - \mathbf{r}_i^0 \right) \otimes \nabla_i^0 W_{ij} \right)^{-1} \qquad (9)$$
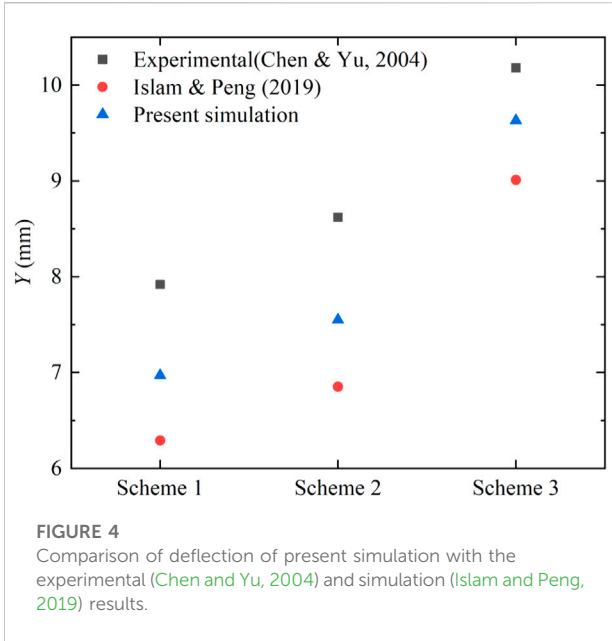
where

$$\nabla_i^0 W_{ij} = \frac{\partial W\left(\left| \mathbf{r}_{ij}^0 \right|, h \right)}{\partial \left| \mathbf{r}_{ij}^0 \right|} \mathbf{e}_{ij}^0 \qquad (10)$$

represents the gradient of the kernel function at the initial reference configuration. It is worth noting that the correction matrix is calculated in the initial configuration and therefore is calculated only once at the beginning of the simulation. Then, the mass and momentum conservation equations can be discretized as

$$\begin{cases} \rho_i = \rho^0 \dfrac{1}{\det(\mathbf{F})} \\ \dfrac{d\mathbf{v}_i}{dt} = \dfrac{2}{m_i} \sum_j V_i V_j \tilde{\mathbf{P}}_{ij} \nabla_i^0 W_{ij} + \mathbf{g} \end{cases} \qquad (11)$$

where the average first Piola-Kirchhoff stress between particles is defined as

$$\tilde{\mathbf{P}}_{ij} = \frac{1}{2} \left(\mathbf{P}_i \mathbf{B}_i^0 + \mathbf{P}_j \mathbf{B}_j^0 \right) \qquad (12)$$

FIGURE 4
Comparison of deflection of present simulation with the experimental (Chen and Yu, 2004) and simulation (Islam and Peng, 2019) results.

and the first Piola-Kirchhoff stress tensor is calculated from the constitutive law with the deformation tensor $\mathbf{F}$, which links initial and current configuration is defined as

$$\mathbf{F} = \left(\sum_j V_j \left(\mathbf{s}_j - \mathbf{s}_i \right) \otimes \nabla_i^0 W_{ij} \right) \mathbf{B}_i^0 + \mathbf{I} \tag{13}$$

Coupling scheme of WC-TLSPH

In the FSI framework, the force of the solid structure on the fluid needs to be considered, so the governing equations of fluid dynamics are expressed as
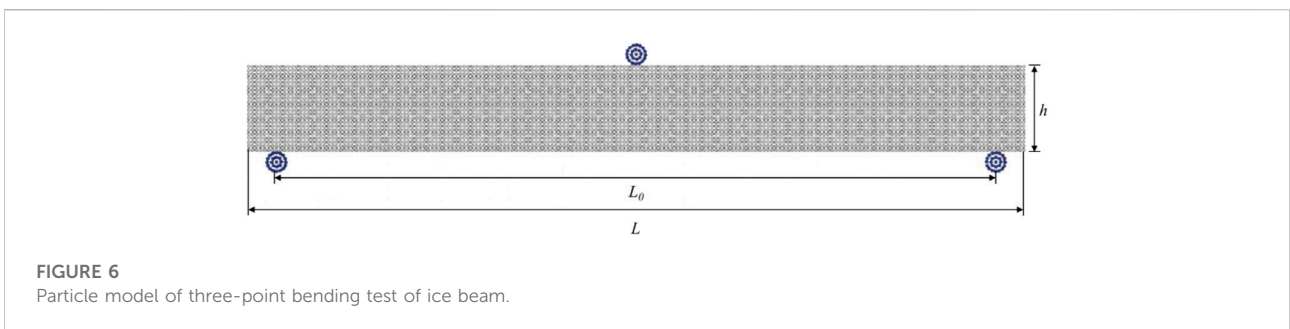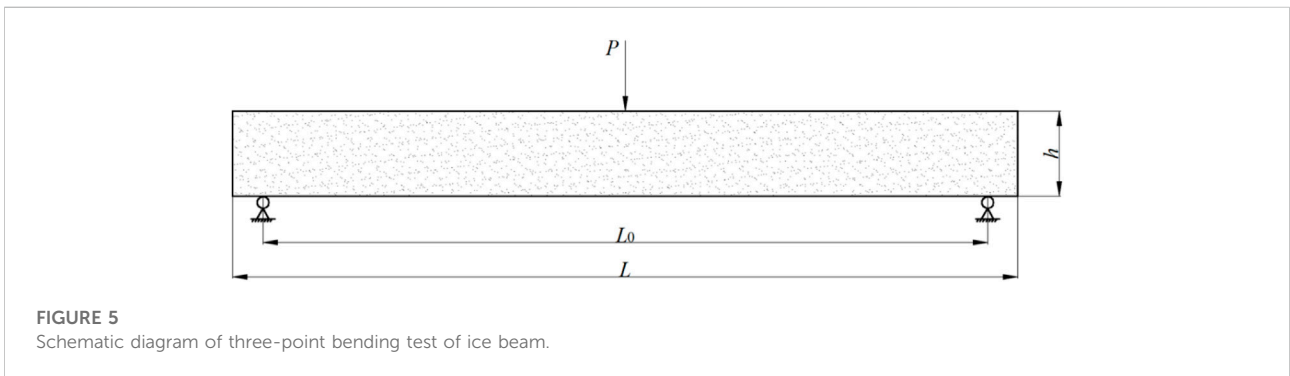
$$\begin{cases} \dfrac{d\rho_i}{dt} = 2\rho_i \sum_j \dfrac{m_j}{\rho_j} \left(U^\star - \mathbf{v}_i \mathbf{e}_{ij} \right) \dfrac{\partial W_{ij}}{\partial r_{ij}} \\[3mm] \dfrac{d\mathbf{v}_i}{dt} = -2\sum_j m_j \dfrac{P^\star}{\rho_i \rho_j} \nabla_i W_{ij} + \mathbf{g} + \mathbf{f}_i^{S:\,p} + \mathbf{f}_i^{S:\,v} \end{cases} \tag{14}$$

where $\mathbf{f}_i^{S:\,p}$ and $\mathbf{f}_i^{S:\,v}$ are the pressure and viscous forces exerted by solid structure on fluid particle, respectively. Similarly, the discretization of the solid dynamics equation is modified as

$$\begin{cases} \rho_a = \rho_0 \dfrac{1}{\det(\mathbf{F})} \\[3mm] \dfrac{d\mathbf{v}_a}{dt} = \dfrac{2}{m_a} \sum_b V_a V_b \tilde{\mathbf{P}}_{ab} \nabla_a^0 W_{ab} + \mathbf{g} + \mathbf{f}_a^{F:\,p} + \mathbf{f}_a^{F:\,v} \end{cases} \tag{15}$$

also $\mathbf{f}_a^{F:\,p}$ and $\mathbf{f}_a^{F:\,v}$ are the fluid pressure and viscous forces acting on the solid particle, respectively. Figure 1 specifies the details of the WC-TLSPH scheme.

In FSI, the surrounding solid structure is behaving as a moving boundary of the fluid, while no-slip boundary condition is imposed at the fluid-structure interface (Zhang et al., 2021a). The solid forces $\mathbf{f}_i^{S:\,p}$ and $\mathbf{f}_i^{S:\,v}$ acting on fluid of Eq. 14 can be calculated by
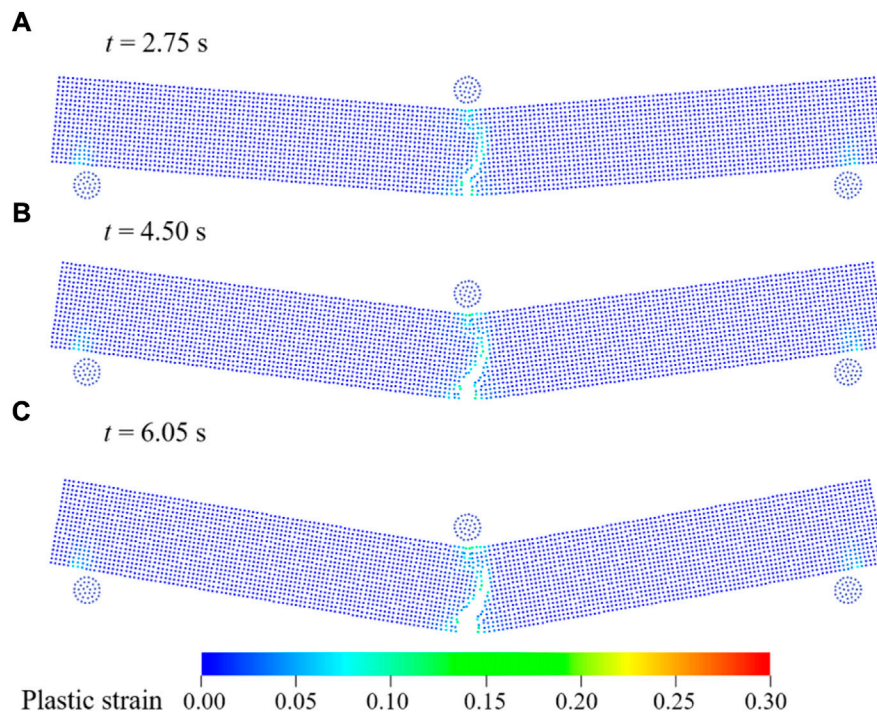

FIGURE 5
Schematic diagram of three-point bending test of ice beam.

FIGURE 6
Particle model of three-point bending test of ice beam.

FIGURE 7
Snapshots of the ice beam in three-point bending experiment by SPH at **(A)** t = 2.75s, **(B)** t = 4.50s and **(C)** t = 6.05s.
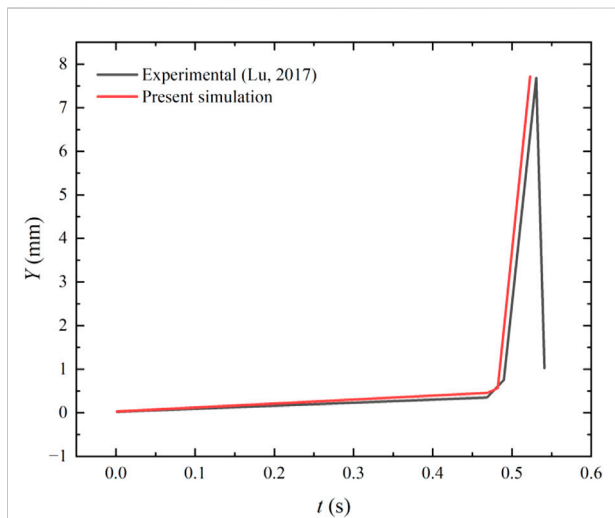

FIGURE 8
Comparison of deflection of present simulation with the experimental (Lu, 2017) results.

TABLE 3 The system and discretization parameters.

Parameters	Value (m)
Water length (L)	0.146
Water height ($2L$)	0.292
Baffle length (l)	0.012
Baffle height (h)	0.080
Box length	0.584
Box height	0.600
Particle spacing	0.0025

$$\mathbf{f}_i^{S:\,v} = 2\sum_a \eta V_i V_a \frac{\mathbf{v}_i - \mathbf{v}_a^d}{|\mathbf{r}_{ia}| + 0.01h} \frac{\partial W(\mathbf{r}_{ia}, h)}{\partial r_{ia}} \qquad (17)$$

where the imaginary particle density ρ_a^d is calculated through the EoS presented in Eq. 2, the coefficient of η is relative with the fluid viscosity, the imaginary pressure p_a^d and velocity $\mathbf{v}_a^d$ are calculated by

$$p_a^d = p_i + \rho_i \max\left(0, \left(\mathbf{g} - \frac{\mathrm{d}\mathbf{v}_a}{\mathrm{d}t}\right) \cdot \mathbf{n}^S\right)(\mathbf{r}_{ia} \cdot \mathbf{n}^S) \qquad (18)$$

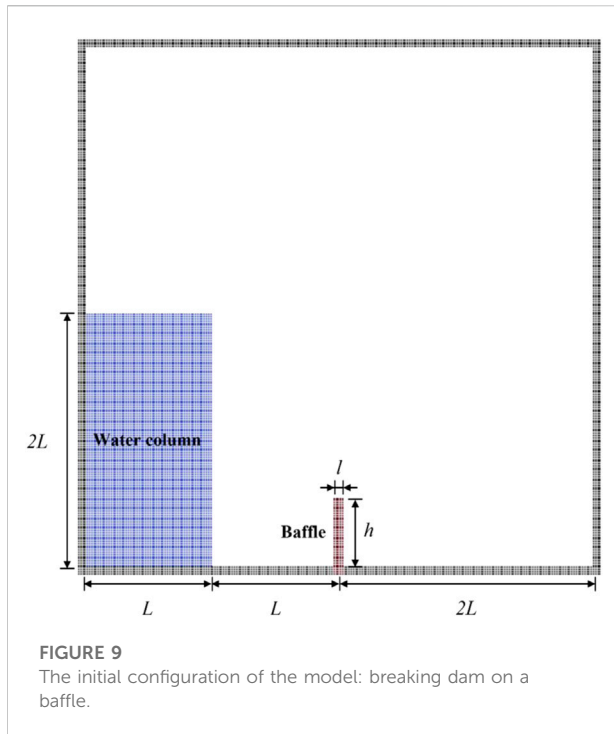$$\mathbf{v}_a^d = 2\mathbf{v}_i - \mathbf{v}_a \qquad (19)$$

$$\mathbf{f}_i^{S:\,p} = -2\sum_a V_i V_a \frac{p_i \rho_a^d + p_a^d \rho_i}{\rho_i + \rho_a^d} \nabla_i W(\mathbf{r}_{ia}, h) \qquad (16)$$

FIGURE 9
The initial configuration of the model: breaking dam on a baffle.

where $\mathbf{n}^S$ denotes the surface normal direction of the solid structure. Similarly, the interaction forces $\mathbf{f}_a^{F:\ p}$ and $\mathbf{f}_a^{F:\ v}$ acting on a solid particle a are given by

$$\mathbf{f}_a^{F:\ p} = -2 \sum_i V_a V_i \frac{p_a^d \rho_i + p_i \rho_a^d}{\rho_i + \rho_a^d} \nabla_a W(\mathbf{r}_{ai}, h) \qquad (20)$$

$$\mathbf{f}_a^{F:\ v} = 2 \sum_i \eta V_a V_i \frac{\mathbf{v}_a^d - \mathbf{v}_i}{|\mathbf{r}_{ai}| + 0.01h} \frac{\partial W(\mathbf{r}_{ai}, h)}{\partial r_{ai}} \qquad (21)$$

In order to ensure momentum conservation and force-calculation matching of FSI, a single time step

$$\Delta t = \min\left(0.25 \min\left(\frac{h}{c^F + |\mathbf{v}|_{\max}}, \frac{h^2}{\eta} \right), 0.6 \min\left(\frac{h}{c^S + |\mathbf{v}|_{\max}}, \sqrt{\frac{h}{\left|\frac{d\mathbf{v}}{dr}\right|_{\max}}} \right) \right) \qquad (22)$$

is commonly used, where c^F and c^S are the sound speed of fluid and solid, respectively. However, this may lead to low computational efficiency since a very small time-step will be chosen when the sound speed of the solid structure is significantly larger than that of the fluid.

Fracture model for TLSPH

As discussed in the previous part, the TLSPH method applies the initial reference configuration for constructing particle configuration, including particle neighbor search and calculation of kernel function and its gradient, and keep it unaltered during the simulation. Therefore, additional

treatment is necessary when applying TLSPH to resolve the fracture problem in solid mechanics.

Considering that the particle interaction in the SPH method is determined by the kernel function, the strength of the particle interaction can be adjusted by introducing a damage factor to the kernel function. Then, the material fracture can be resolved by adopting the damage factor according to fracture rule as pointed out by Islam and Peng (2019). The specific calculation process can be achieved through the following steps: firstly, establishing a virtual chain between the interacting particles. Here, the function of the virtual chain is to store the strength of particle interaction without providing any additional stiffness. Secondly, introducing the particle damage factor D to define the damage degree of material particles according to the plastic strain as

$$D = \begin{cases} 1, & \varepsilon_{pl} \geq (\varepsilon_{pl})_{\max} \\ 0, & \text{otherwise} \end{cases} \qquad (23)$$

where $(\varepsilon_{pl})_{max}$ is the maximum plastic strain of the material and determined by its mechanical property. Finally, calculate the interparticle damage factor $f_{ij} = 1 - D_{ij}$ to modify the kernel function and its gradient of the particle at the fracture. According to the formula, when $f_{ij} = 1$ the virtual chain between particles is not destroyed, and when $0 < f_{ij} < 1$ the virtual chain is partially destroyed, while when $f_{ij} = 0$ the virtual chain is completely destroyed. Then the momentum conservation equation in the TLSPH formulation can be rewritten as

$$\frac{d\mathbf{v}_i}{dt} = \frac{2}{m_i} \sum_{j \in N_U^i} V_i V_j \tilde{\mathbf{P}}_{ij} \nabla_i^0 W_{ij} + \frac{2}{m_i} \sum_{j \in N_D^i} V_i V_j \tilde{\mathbf{P}}_{ij} f_{ij} \nabla_i^0 W_{ij} \qquad (24)$$

where N_U^i and N_D^i are the sets of neighboring particles connected to the particle i through the undamaged and damaged virtual chains, respectively.

Model validation and application

In this section, the adopted fractural model for the TLSPH method is first validated by two benchmark tests, *viz.* crack propagation in notched beam and three-point bending of ice beam. Then, a test of dam break flow impacting on a structure with and without fractural model is investigated to study the accuracy, robustness and versatility of the proposed coupled WC-TLSPH method.

Fast-loading case crack propagation in notched beam

The fast-loading fracture case is firstly verified by considering a projectile impacting aluminum beam, as shown in Figure 2, where experimental data of Chen and Yu (2004) and numerical results of Islam and Peng (2019) are available for quantitative comparison.
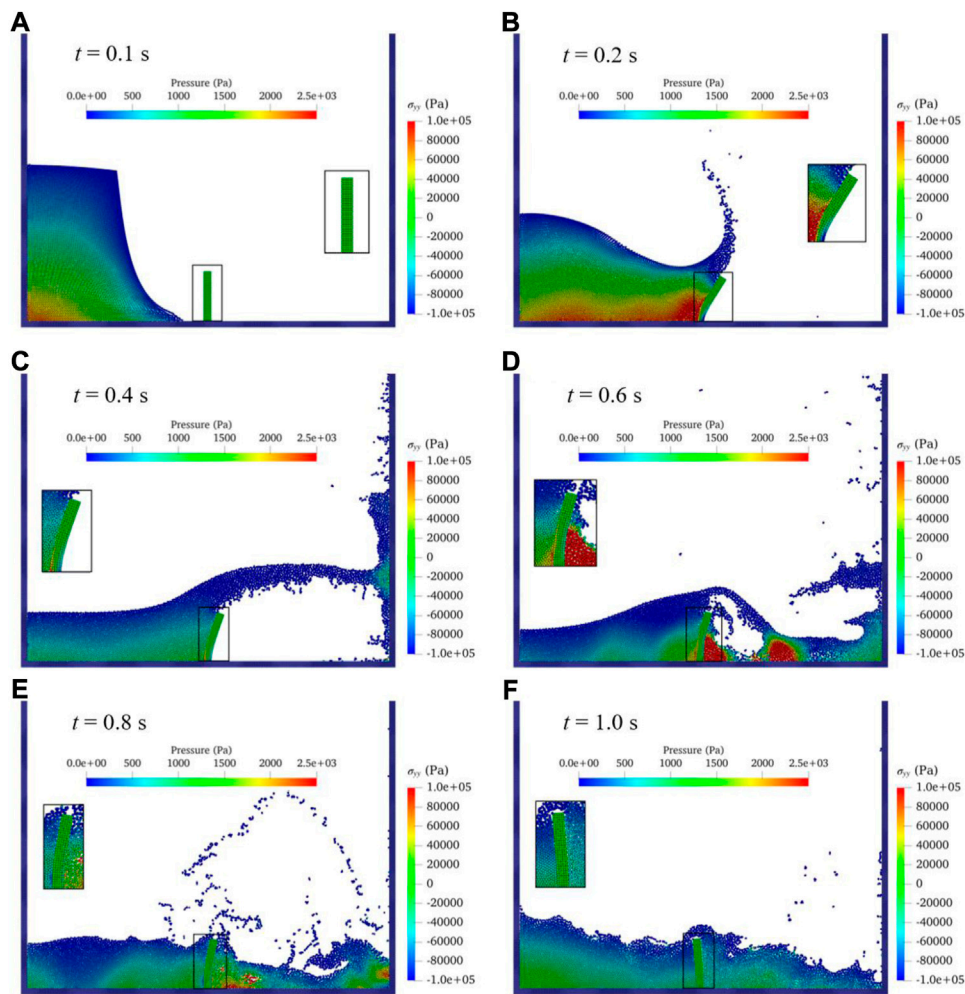
FIGURE 10
Contours of water pressure, surface profile and σ_{yy} of elastic baffle at **(A)** t = 0.1s, **(B)** t = 0.2s, **(C)** t = 0.4s, **(D)** t = 0.6s, **(E)** t = 0.8s and **(F)** t = 1.0s.

Following Chen and Yu (2004), the size of the aluminum beam is 142.24 × 6.35 mm and the I-type notch or II-type notch (the I-type notch is of 2.12 mm high and 0.8 mm wide, and the II-type notch is of 2.12 mm high and 1.5 mm wide) is preset in the middle and with fixed constraints being imposed on both ends.
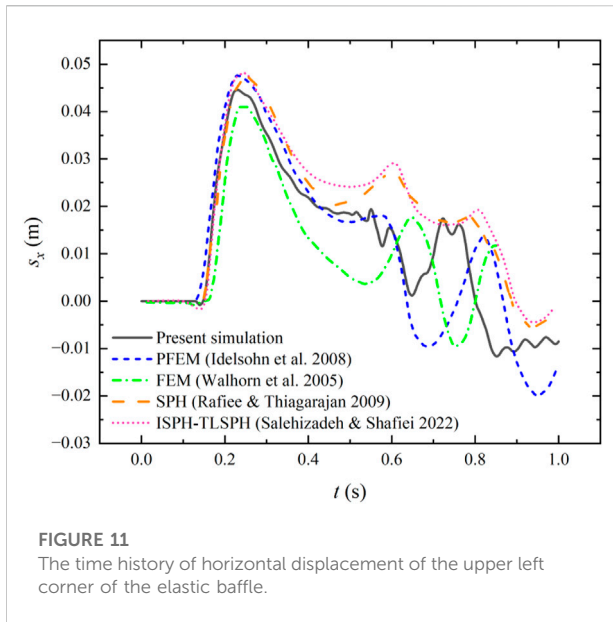
The material properties of the aluminum beam are given in Table 1. The aluminum beam was impacted with a projectile to study the deformation and fracture phenomena of the aluminum beam. Note that the size of the projectile is of 50.00 × 14.74 mm.

Also, the simulation scheme sets four working conditions according to the literature and the detailed parameters are shown in Table 2.

To discretize the system, the particle spacing is set to 0.423 mm and the total number of particles is 12,906 including 8,894 particles for aluminum beam and 4,012 particles for projectile. The von Mises criterion is selected for the yield criterion, defined as $y_f = \sqrt{J_2} - \sigma_y/\sqrt{3}$, where σ_y is the yield stress of material and

J_2 is the second invariant of the deviatoric stress tensor. According to the criterion, when $y_f \leq 0$ the material is in the elastic stage, and when $y_f > 0$ the material enters the plastic stage. And the plastic hardening model (Simo and Hughes, 2006) is applied to the constitutive model.

The simulation results are shown in Figure 3. The first column is the experimental results of Chen and Yu (2004), the second is the simulation results of Islam and Peng (2019) and the third is the present simulation. Under the four different initial impact velocities, the present model can better reflect the bending and fracture of the aluminum beam in comparison with those of Islam and Peng (2019). From the perspective of plastic strain distribution, the present results and those of Islam and Peng's (2019) show the same law. However, there are discrepancies can be noted, *e.g.* the present results show the plastic strain at middle part of the aluminum beam is slightly smaller than the results of Islam and Peng (2019) when the aluminum beam is not broken, but significantly larger than the results of Islam and Peng

FIGURE 11
The time history of horizontal displacement of the upper left corner of the elastic baffle.

(2019) after the aluminum beam breaks. The reason for this phenomenon may be due to that the choice of different material constitutive model in the simulation.

In Figure 4, the present results are compared with the experimental observation of the deflection in Y-axis of the aluminum beam in Schemes 1-3. It can be seen from the results that the present results have a good agreement with the experimental results under different initial impact velocities. Quantitatively, the relative errors in the 3 schemes of present simulation are 11.99, 12.41 and 5.40%, respectively.

Slow-loading case three-point bending of ice beam

The slow-loading fracture case is verified by considering a three-point bending an ice beam, which is also studied by Lu (2017). The initial configuration is shown in Figure 5 where the size of the simply supported ice beam is 650 mm × 70 mm and the distance between the fixed ends on both sides 600 mm. Also, the loading speed of the point pressure is 0.763 mm/s.

To discretize the system as show in Figure 6, the particle spacing is set to Δx = 3.5 mm, resulting a total number of 3,720 particles. The plastic hardening constitutive model and the von Mises yield criterion are also applied herein. The mechanical properties of the ice material refer to Lu's work (Lu, 2017) where the density ρ = 896.977 kg/m³, the elastic modulus E = 6.81 GPa and the Poisson's ratio υ = 0.33. The CPU time on an Intel(R) Xeon(R) Gold 6136 CPU @ 3.00 GHz computer are 7.06 h for 22,600,000 computational steps to simulate a physical process of 10 s.

Figure 7 shows the present results of the crack and its propagation during the loading process with the particles colored by the plastic strain contour. At t = 2.75 s, obvious cracks can be observed. At the same time, pronounced strain aera appear at the support of the beam and the compression and tension areas of the loader. As the loading process continues, the cracks gradually expand meanwhile the range of strain aera also increases slightly. When the time reaches t = 6.05 s, the crack expands to a certain extent and an obvious fracture surface appears, noting the increase of strain at the fracture. The present results herein show the same trend as those of Zhang et al. (2019), including the fracture degree and fracture location of the ice beam at each frame. However, detailed comparison is not conducted in this paper due to the slight differences in the model parameters.

In order to verify the accuracy of the present results under slow-loading, the deflection at the midpoint of the ice beam is compared with the experimental data in the literature (Lu, 2017) in Figure 8 where the deflection is represented by Y. The simulation results tend to be consistent with the experimental results. Before fracture, the deflection increases linearly with time. At t = 0.49 s, the ice beam breaks and the deflection increases significantly. However, the simulation results show a slightly larger deflection than the experimental data, and meanwhile fracture is also advanced probably because the maximum plastic strain $(\varepsilon_{pl})_{max}$ chosen in the simulation process is slightly different from the actual situation of the ice material.

FSI case breaking dam on an elastic/ elastoplastic baffle

In this section, the case of breaking dam impacting on an elastic/elastoplastic baffle, in which a column of water collapses and influences on an elastic or elastoplastic baffle, is established to study the difference and response of elastic and elastoplastic materials under the impacting load of water flow. As shown in Figure 9, a column of water confined at the left end of the container is initially in hydrostatic equilibrium state and an elastic/elastoplastic baffle is attached to the bottom of the tank with one end free. The parameters of this test case are listed in Table 3.

The initial density of water and the baffle are set to 1,000 kg/m³ and 2,500 kg/m³, respectively. Other parameters for the baffle are Young's modulus E = 1.0 MPa and Poisson ratio υ = 0. The elastic baffle is modeled using the linear elastic constitutive model and the elastoplastic baffle using the plastic hardening constitutive model. In addition, in simulating the deformation and failure process of elastoplastic baffle, the von Mises yield criterion is also applied and the fracture model established in this paper is coupled. The convergence analysis of the model is shown in
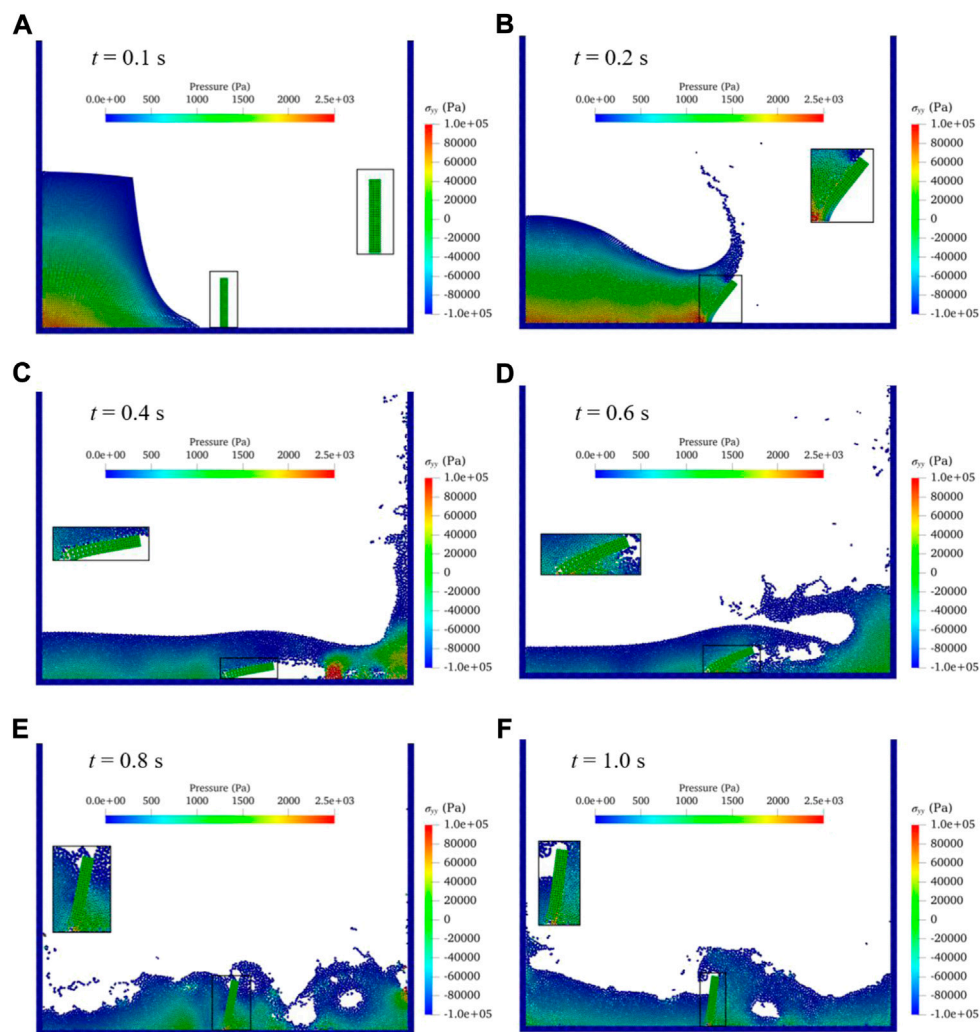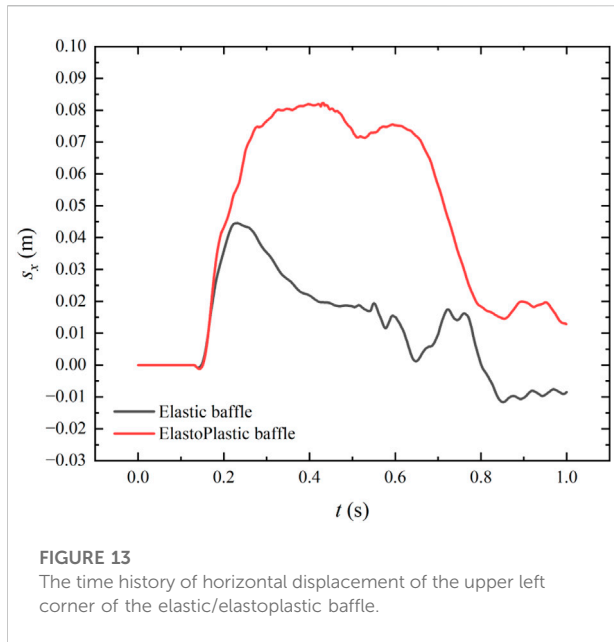
FIGURE 12
Contours of water pressure, surface profile and σ_{yy} of elastoplastic baffle at **(A)** t = 0.1s, **(B)** t = 0.2s, **(C)** t = 0.4s, **(D)** t = 0.6s, **(E)** t = 0.8s and **(F)** t = 1.0s.

the Appendix. The particle spacing is set to Δx = 2.5mm, resulting a total number of 10,820 particles are used in the simulation, including 6,785 fluid particles, 3,855 boundary particles and 180 solid particles. The CPU time on an 11th Gen Intel(R) Core (TM) i9-11900K @ 3.50 GHz computer are 2.78 min for 26,100 computational steps to simulate a physical process of 10.0 s.

The free-surface profile with pressure contour and the deformed configuration of the elastic baffle are shown in Figure 10A, corresponding to the flow state at t = 0.1s, t = 0.2s, t = 0.4s, t = 0.6s, t = 0.8s and t = 1.0s, respectively. Also, the figure shows a partial enlarged view of the distributions of stress component on the y-axis σ_{yy} in the elastic baffle. As the water column is released, the water naturally flows with gravity. Before reaching the elastic baffle, its pressure

distribution conforms to the pressure distribution law of normal water flow, *viz.* the pressure is the largest at the lower left corner. When the water flow reaches the position of the elastic baffle and interacts with the elastic baffle at t = 0.2s, the falling water flow makes the elastic baffle tilt to the right and generates a large stress at the root of the elastic baffle, and the water pressure is also close to the maximum value at the position of the elastic baffle reaches. Then the water flow passes over the elastic baffle and the deformation of the elastic plate gradually recovers, imposing an ejection effect on the water flow. With the weakening of the energy of water flow and elastic baffle, the water pressure gradually tends to the distribution of the hydrostatic pressure, and the elastic baffle gradually returns to the initial state. The simulation results of the above part are in good agreement

FIGURE 13
The time history of horizontal displacement of the upper left corner of the elastic/elastoplastic baffle.

with the simulation results of Zhan et al (2019) which presents the same study in three-dimensional using a stabilized TL–WCSPH approach with GPU acceleration.

Figure11 shows the time history of horizontal displacement of the upper left corner of the elastic baffle where horizontal displacement is represented by s_x. Several simulation results of PFEM (Idelsohn et al., 2008), FEM (Walhorn et al., 2005), SPH (Rafiee and Thiagarajan, 2009) and incompressible SPH (ISPH) -TLSPH (Salehizadeh and Shafiei, 2022) from literature are also given for comparison. It can be seen from the figure that the maximum displacement time of the elastic baffle in this paper is similar to the simulation results in the literatures, and the amplitude and frequency of the elastic baffle oscillation show basically the same trend as those in the literature and the present results is within the range of the above literature results. In addition, it can be seen that the simulation in this paper can better reflect the motion details of the elastic baffle.

Through the above analysis, the present WC-TLSPH has good accuracy in FSI simulation, and the fracture model based on TLSPH can simulate the fracture process of the material well. Therefore, it can also corroborate the WC-TLSPH model coupled with fracture model to simulate the failure process of the structure in the FSI.

Figure 12 shows the free-surface profile with water pressure contour and the deformation of the elastoplastic baffle, (a)-(f) corresponding to the flow state at $t = 0.1s$, $t = 0.2s$, $t = 0.4s$, $t = 0.6s$, $t = 0.8s$ and $t = 1.0s$ respectively. The figure also shows a partial enlarged view of the distributions of stress σ_{yy} in the elastoplastic baffle. As the water column is released, the water naturally flows with gravity. Before reaching the elastoplastic

baffle, its pressure exhibits the same distribution as in the elastic baffle case. When the water flow reaches the position of the elastoplastic baffle, the baffle is tilted to the right significantly more than the elastic baffle, at $t = 0.4s$, the impact of the downward water flow causes obvious plastic damage to the root of the elastoplastic baffle. Compared with the elastic baffle, in this case, the baffle has lost the ability to rebound and eject the water, so the concentration point of the water pressure is mainly at the drop of the water flow. Then, with the backflow generated after the water flow reaches the right boundary, the displacement of the baffle gradually recovers. However, the connection between the baffle root and the boundary tends to be destroyed completely, leading to the lack of restraint at the root, the baffle basically does not have obvious deformation, which is closely related to the water flow. The interaction with the water flow is also mainly reflected in the buoyancy effect of the water flow on the baffle, and the pressure distribution of the water flow basically shows the distribution characteristics of the hydrostatic pressure.

Figure13 shows the time history of horizontal displacement of the upper left corner of the elastic baffle and elastoplastic baffle. It can be seen that before $t = 0.18$ s, i.e., before the elastoplastic baffle reaches the plastic state, the displacement of the baffle in the two cases shows the same tendency, and then is significantly larger than that of the elastic baffle, although there is a lack of experimental data verification, from a qualitative point of view this is also in line with the common sense. In addition, compared with the displacement change of the elastic baffle, another significant difference in the displacement of the elastoplastic baffle is the lack of reciprocating motion in the displacement due to the lack of rebound effect.

Through the above comparative analysis, the method used in this paper can accurately simulate the deformation and failure process of the structure in FSI. Although the verification of experimental data is lacking in this process, combined with previous research experience, the simulation results of the flow process and pressure distribution of the water flow, as well as the stress distribution and movement trend of the baffle plate have good accuracy.

Conclusion

Based on the WC-TLSPH model in the SPHinXsys library, a fracture model is established to simulate the failure process of the structure in FSI. The fluid phase was simulated by the WCSPH method, the solid phase was simulated by the TLSPH method to reduce the influence of tensile instability, the fracture of the material was achieved by introducing a damage factor for kernel function correction. By comparing the numerical results of the fast-loading case of crack propagation in notched beam and the slow-loading case

of three-point bending of ice beam with the experimental data in the literature, the accuracy of the simulation results of the fracture model in different working conditions is verified respectively. The comparison with literature data demonstrates the accuracy and robustness of the WC-TLSPH model in FSI simulations. The above model verification can also corroborate the simulation results of the breaking dam on an elastoplastic baffle to a certain extent. The results show that the method of introducing the damage factor to modify kernel function can well realize the fracture model based on TLSPH, which solves the problem that TLSPH cannot simulate the fracture process naturally. The coupling of the WC-TLSPH model and the fracture model can simulate the fracture process of the structure in the case of FSI well and provide a certain reference for practical engineering applications.

This might be the first time that SPHinXsys is used for fracture of solid structures and there is no quantitative data of physical experiment for a comparison, so the depth of study is still relatively shallow. In the manuscript we tried to provide a few quantitative validations, but it seems quite insufficient. A series of more challenging benchmark tests are being carried out now and will be presented in future work.

Data availability statement

The raw data supporting the conclusions of this article will be made available by the authors, without undue reservation.

Author contributions

HW: methodology, simulation, visualization, validation, analysis, and writing—original draft. SG: supervision, conceptualization, management, and writing—review and editing. LT: investigation and writing—review and editing. JL: investigation and writing—review and editing. CC: investigation and writing—review and editing. CZ: supervision, conceptualization, management, and writing—review and editing. All authors contributed to the article and approved the submitted version.

Conflict of interest

The authors declare that the research was conducted in the absence of any commercial or financial relationships that could be construed as a potential conflict of interest.

Publisher's note

All claims expressed in this article are solely those of the authors and do not necessarily represent those of their affiliated organizations, or those of the publisher, the editors and the reviewers. Any product that may be evaluated in this article, or claim that may be made by its manufacturer, is not guaranteed or endorsed by the publisher.

References

Belytschko, T., Guo, Y., Kam Liu, W., and Ping Xiao, S. (2000). A unified stability analysis of meshless particle methods. *Int. J. Numer. Methods Eng.* 48 (9), 1359–1400. doi:10.1002/1097-0207(20000730)48:9<1359::AID-NME829>3.0.CO;2-U

Bui, H. H., Fukagawa, R., Sako, K., and Ohno, S. (2008). Lagrangian meshfree particles method (SPH) for large deformation and failure flows of geomaterial using elastic–plastic soil constitutive model. *Int. J. Numer. Anal. Methods Geomech.* 32 (12), 1537–1570. doi:10.1002/nag.688

Chen, F., and Yu, T. (2004). An experimental study of pre-notched clamped beams under impact loading. *Int. J. solids Struct.* 41 (24-25), 6699–6724. doi:10.1016/j.ijsolstr.2004.05.036

Gabreil, E., Wu, H., Chen, C., Li, J., Rubinato, M., Zheng, X., et al. (2022). Three-dimensional smoothed particle hydrodynamics modeling of near-shore current flows over rough topographic surface. *Front. Mar. Sci.* 9, 935098. doi:10.3389/fmars.2022.935098

Gray, J. P., Monaghan, J. J., and Swift, R. P. (2001). SPH elastic dynamics. *Comput. Methods Appl. Mech. Eng.* 190 (49), 6641–6662. doi:10.1016/S0045-7825(01)00254-7

Gu, S., Zheng, W., Wu, H., Chen, C., and Shao, S. (2022). DualSPHysics simulations of spillway hydraulics: A comparison between single- and two-phase modelling approaches. *J. Hydraulic Res.* 60 (5), 835–852. doi:10.1080/00221686.2022.2064343

He, J., Tofighi, N., Yildiz, M., Lei, J., and Suleman, A. (2017). A coupled WC-TL SPH method for simulation of hydroelastic problems. *Int. J. Comput. Fluid Dyn.* 31 (3), 174–187. doi:10.1080/10618562.2017.1324149

Idelsohn, S. R., Marti, J., Limache, A., and Oñate, E. (2008). Unified Lagrangian formulation for elastic solids and incompressible fluids: Application to fluid–structure interaction problems via the PFEM. *Comput. Methods Appl. Mech. Eng.* 197 (19-20), 1762–1776. doi:10.1016/j.cma.2007.06.004

Islam, M. R. I., and Peng, C. (2019). A Total Lagrangian SPH method for modelling damage and failure in solids. *Int. J. Mech. Sci.* 157-158, 498–511. doi:10.1016/j.ijmecsci.2019.05.003

Johnson, G. R., and Beissel, S. R. (1996). Normalized smoothing functions for SPH impact computations. *Int. J. Numer. Methods Eng.* 39, 27252–27419. doi:10.1002/(SICI)1097-0207(19960830)39:16<2725::AID-NME973>3.0

Lu, W. (2017). The Study of the numerical simulation Method of peridynamic Based on the bending Fracture of sea ice master. China: Harbin Engineering University. Thesis.

Lv, X., Zhao, Y., Huang, X. Y., Xia, G. H., and Su, X. H. (2007). A matrix-free implicit unstructured multigrid finite volume method for simulating structural dynamics and fluid–structure interaction. *J. Comput. Phys.* 225 (1), 120–144. doi:10.1016/j.jcp.2006.11.023

Mitra, S., and Sinhamahapatra, K. P. (2008). 2D simulation of fluid-structure interaction using finite element method. *Finite Elem. Analysis Des.* 45 (1), 52–59. doi:10.1016/j.finel.2008.07.006

Monaghan, J. J. (1992). Smoothed particle hydrodynamics. *Annu. Rev. Astron. Astrophys.* 30, 543–574. doi:10.1146/annurev.aa.30.090192.002551

Morris, J. P., Fox, P. J., and Zhu, Y. (1997). Modeling low Reynolds number incompressible flows using SPH. *J. Comput. Phys.* 136 (1), 214–226. doi:10.1006/jcph.1997.5776

Rafiee, A., and Thiagarajan, K. P. (2009). An SPH projection method for simulating fluid-hypoelastic structure interaction. *Comput. Methods Appl. Mech. Eng.* 198 (33-36), 2785–2795. doi:10.1016/j.cma.2009.04.001

Salehizadeh, A. M., and Shafiei, A. R. (2022). A coupled ISPH-TLSPH method for simulating fluid-elastic structure interaction problems. *J. Mar. Sci. Appl.* 21 (1), 15–36. doi:10.1007/s11804-022-00260-3

Sarrate, J., Huerta, A., and Donea, J. (2001). Arbitrary Lagrangian–Eulerian formulation for fluid–rigid body interaction. *Comput. Methods Appl. Mech. Eng.* 190 (24), 3171–3188. doi:10.1016/S0045-7825(00)00387-X

Shi, H., Si, P., Dong, P., and Yu, X. (2019). A two-phase SPH model for massive sediment motion in free surface flows. *Adv. Water Resour.* 129, 80–98. doi:10.1016/j.advwatres.2019.05.006

Shi, H., Yu, X., and Dalrymple, R. A. (2017). Development of a two-phase SPH model for sediment laden flows. *Comput. Phys. Commun.* 221, 259–272. doi:10.1016/j.cpc.2017.08.024

Simo, J. C., and Hughes, T. J. (2006). *Computational inelasticity*, New York: Springer Science & Business Media.

Sugiyama, K., Ii, S., Takeuchi, S., Takagi, S., and Matsumoto, Y. (2011). A full Eulerian finite difference approach for solving fluid-structure coupling problems. *J. Comput. Phys.* 230 (3), 596–627. doi:10.1016/j.jcp.2010.09.032

Walhorn, E., Kölke, A., Hübner, B., and Dinkler, D. (2005). Fluid–structure coupling within a monolithic model involving free surface flows. *Comput. Struct.* 83 (25-26), 2100–2111. doi:10.1016/j.compstruc.2005.03.010

Zhan, L., Peng, C., Zhang, B., and Wu, W. (2019). A stabilized TL–WC SPH approach with GPU acceleration for three-dimensional fluid–structure interaction. *J. Fluids Struct.* 86, 329–353. doi:10.1016/j.jfluidstructs.2019.02.002

Zhang, C., Hu, X., and Adams, N. A. (2017a). A weakly compressible SPH method based on a low-dissipation Riemann solver. *J. Comput. Phys.* 335, 605–620. doi:10.1016/j.jcp.2017.01.027

Zhang, C., Hu, X. Y., and Adams, N. A. (2017b). A generalized transport-velocity formulation for smoothed particle hydrodynamics. *J. Comput. Phys.* 337, 216–232. doi:10.1016/j.jcp.2017.02.016

Zhang, C., Rezavand, M., and Hu, X. (2021a). A multi-resolution SPH method for fluid-structure interactions. *J. Comput. Phys.* 429, 110028. doi:10.1016/j.jcp.2020.110028

Zhang, C., Rezavand, M., Zhu, Y., Yu, Y., Wu, D., Zhang, W., et al. (2021b). SPHinXsys: An open-source multi-physics and multi-resolution library based on smoothed particle hydrodynamics. *Comput. Phys. Commun.* 267, 108066. doi:10.1016/j.cpc.2021.108066

Zhang, C., Wei, Y., Dias, F., and Hu, X. (2021c). An efficient fully Lagrangian solver for modeling wave interaction with oscillating wave surge converter. *Ocean. Eng.* 236, 109540. doi:10.1016/j.oceaneng.2021.109540

Zhang, C., Zhu, Y., Wu, D., and Hu, X. (2022). Review on smoothed particle hydrodynamics: Methodology development and recent achievement. arXiv preprint arXiv:2205.03074.

Zhang, N., Zheng, X., Ma, Q., and Hu, Z. (2019). A numerical study on ice failure process and ice-ship interactions by Smoothed Particle Hydrodynamics. *Int. J. Nav. Archit. Ocean Eng.* 11 (2), 796–808. doi:10.1016/j.ijnaoe.2019.02.008

Zheng, X., Tian, Z., Xie, Z., and Zhang, N. (2022). Numerical study of the ice breaking resistance of the icebreaker in the yellow river through smoothed-particle hydrodynamics. *J. Mar. Sci. Appl.* 21 (1), 1–14. doi:10.1007/s11804-022-00259-w

Appendix: Convergence analysis

This appendix checks the convergence of WC-TLSPH computation in spatial domain using three different particle sizes, *i.e.*, Δx = 1.5, 2.5, and 3.5 mm, for breaking dam on an elastoplastic baffle. The rest of the model parameters are set the same as the case in the main text. Figure A1 shows that the flow state of the water, the distribution of water pressure, the pouring degree and distributions of stress component on the y-axis σ_{yy} of the elastoplastic baffle are basically the same under three different particle spacings at t = 0.4 s.

Figure A2 reveal a good overlapping behavior of horizontal displacement of the upper left corner of the elastoplastic baffle for the three different particle spacings, indicating the convergence of numerical results.
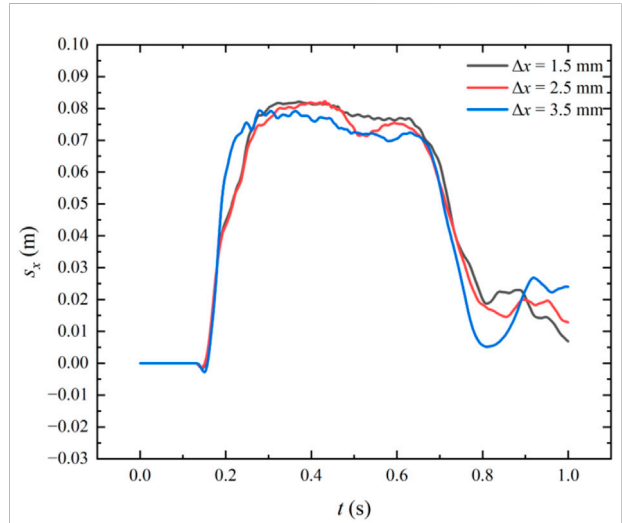

FIGURE A2
The time history of horizontal displacement of the upper left corner of the elastoplastic baffle.
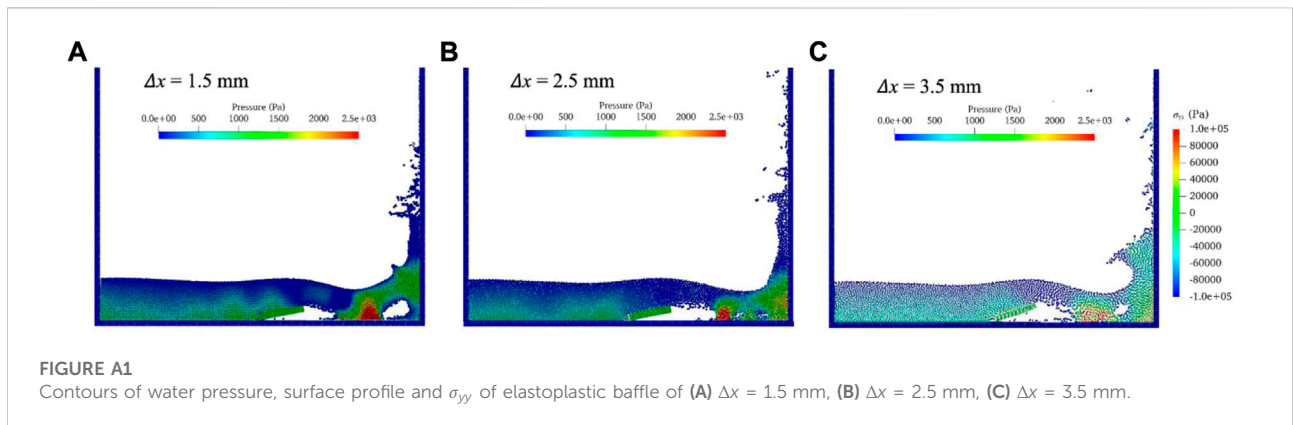

FIGURE A1
Contours of water pressure, surface profile and σ_{yy} of elastoplastic baffle of **(A)** Δx = 1.5 mm, **(B)** Δx = 2.5 mm, **(C)** Δx = 3.5 mm.